


X-ray intraday variability of the TeV blazar Mrk 421 with *Chandra*

Vishi Aggrawal,^{1★} Ashwani Pandey,^{1,2★} Alok C. Gupta ,^{1★} Zhongli Zhang,³
Paul J. Wiita,⁴ K. K. Yadav⁵ and S. N. Tiwari²

¹Aryabhata Research Institute of Observational Sciences (ARIES), Manora Peak, Nainital 263002, India

²Department of Physics, DDU Gorakhpur University, Gorakhpur 273009, India

³Shanghai Astronomical Observatory, Chinese Academy of Sciences, 80 Nandan Road, Shanghai 200030, China

⁴Department of Physics, The College of New Jersey, 2000 Pennington Road, Ewing, NJ 08628-0718, USA

⁵Astrophysical Sciences Division, Bhabha Atomic Research Centre, Mumbai 400085, India

Accepted 2018 August 7. Received 2018 August 7; in original form 2017 October 25

ABSTRACT

We present an extensive study of 72 archival *Chandra* light curves of the high-frequency-peaked type blazar Mrk 421, the first strong extragalactic object to be detected at TeV energies. Between 2000 and 2015, Mrk 421 often displayed intraday variability in the 0.3–10.0 keV energy range, as quantified through fractional variability amplitudes that range up to 21.3 per cent. A variability duty cycle of ~ 84 per cent is present in these data. Variability time-scales, with values ranging from 5.5 to 30.5 ks, appear to be present in seven of these observations. Discrete correlation function analyses show positive correlations between the soft (0.3–2.0 keV) and hard (2.0–10.0 keV) X-ray energy bands with zero time lags, indicating that very similar electron populations are responsible for the emission of all the X-rays observed by *Chandra*. The hardness ratios of this X-ray emission indicate a general ‘harder-when-brighter’ trend in the spectral behaviour of Mrk 421. Spectral index–flux plots provide model-independent indications of the spectral evolution of the source and information on the X-ray emission mechanisms. Brief discussions of theoretical models that are consistent with these observations are given.

Key words: galaxies: active – BL Lacertae objects: general – BL Lacertae objects: individual: Mrk 421.

1 INTRODUCTION

An active galactic nucleus (AGN) involves a supermassive black hole (SMBH), fuelled by an accretion disc, producing a variety of highly energetic phenomena (Rees 1984). When a radio-loud AGN is viewed with one of its relativistic jets in close proximity ($\leq 10^\circ$) to our line of sight (LOS), it is categorized as a blazar (Urry & Padovani 1995). Blazars club together BL Lacertae objects, which have nearly featureless optical continua and many flat spectrum radio quasars (FSRQs) that show extensive broad emission lines (e.g. Agarwal et al. 2015). Blazars are observed to be particularly violent AGNs, involving multiple outstanding attributes, including dominance of non-thermal emission, high polarization, extreme flux variability across the entire electromagnetic (EM) spectrum, core-dominated radio morphology, and flat radio spectrum. All of these can be understood in terms of relativistic motion of plasma in the jets and Doppler boosting (e.g. Gaur, Gupta & Wiita 2012a; Agarwal et al. 2016). The high polarization (> 3 per cent) of their radio to

optical emission means that the synchrotron emission mechanism is responsible for broad-band non-thermal EM radiations from blazars at lower frequencies (radio through the UV or X-ray bands), while at higher frequencies it is likely to be dictated by inverse Compton (IC) scattering of seed photons by the same electrons producing the synchrotron emission. Blazar spectral energy distributions (SEDs) demonstrate a double-peak structure (e.g. Gaur et al. 2012a). The low energy peaked blazars (LBLs) have the first SED bump peak in mm to optical bands and the second bump at GeV energies, while the high energy peaked blazars (HBLs) have the first component peak at UV/X-ray, while the second ranges up to TeV energies (Finke & Becker 2014). The BL Lac/FSRQ subclasses also can be distinguished based on optical polarization properties: BL Lac objects show an amplified polarization towards the blue, probably arising due to some intrinsic phenomenon related to the jet-emitting region (Stocke et al. 1991; Marcha et al. 1996), while the FSRQs trend in the opposite direction, possibly because of significant contributions from the unpolarized quasi-thermal emission from the accretion disc and surrounding region.

Blazar observations often show detectable flux variations down to time periods of a few minutes to hours; these must arise from acute physical conditions within small, subparsec scale, regions

* E-mail: vishiaggrawal.12@gmail.com (VA); ashwanitapan@gmail.com (AP); acgupta30@gmail.com (ACG)

(e.g. Gupta et al. 2016a). Blazar variability is conveniently sectioned into three classes, based on their observed time-scales: flux changes occurring over a time-scale of a day or less and up to a few hundredths of a magnitude are termed as intraday variability (IDV) (Wagner & Witzel 1995), or microvariability (Miller, Carini & Goodrich 1989), or intranight variability (Gopal-Krishna, Sagar & Wiita 1993); variations in flux, typically of a few tenths of a magnitude, that extend from days to weeks are known as short-term variability (STV); while variations ranging from several months to a few years are called long-term variability (LTV) (Gupta et al. 2004). Extensive studies of STV and LTV for blazars have often shown variations exceeding ~ 1 mag and some have spanned over ~ 5 mag. These flux variabilities in blazars could either be initiated through unstable accretion disc phenomena or solely through changes in the Doppler-boosted emission of the relativistic jets (Ulrich, Maraschi & Urry 1997). Studies of variability time-scales and amplitudes serve as key tools in understanding physical processes in the jets and the sizes and locations of the emission regions in AGN.

1.1 Mrk 421

Markarian 421 (B2 1101+38; Mrk 421 hereafter) is a nearby elliptical active galaxy ($\alpha_{2000} = 11^{\text{h}}04^{\text{m}}27.3139^{\text{s}}$ and $\delta_{2000} = +38^{\circ}12'31.7991''$) with an intense point-like nucleus, encompassing an $\sim 3.6 \times 10^8 M_{\odot}$ black hole (Wagner 2008). The nuclear source is classified as of the BL Lacertae type as it has a featureless optical spectrum, strongly polarized and variable optical and radio fluxes, and compact radio emission. Mrk 421 has a SED well characterized by a classic two-peak shape (Urry & Padovani 1995; Ulrich et al. 1997). Most of these observed properties of Mrk 421 are understood to arise from a relativistic jet spotted at a small angle to our LOS (Urry & Padovani 1995). Relativistic electrons radiating via the synchrotron process produce a non-thermal SED with a polarized continuum extending from the radio to the soft X-ray bands.

Mrk 421 ($z = 0.031$) is one of the closest blazars, at a distance of 134 Mpc ($H_0 = 71 \text{ km s}^{-1} \text{ Mpc}^{-1}$, $\Omega_m = 0.27$, $\Omega_{\Lambda} = 0.73$) and its synchrotron emission peak was long ago found to lie in the range of 0.1 keV to several keV (Punch et al. 1992). The Whipple Cherenkov Telescope claimed to have detected this extragalactic source at TeV energy range (0.5–1.5 TeV) (Schubnell et al. 1993) and it has been confirmed as a TeV source by multiple ground-based γ -ray telescopes (e.g. Abeysekara et al. 2017). The *Compton Gamma-Ray Observatory* (CGRO) easily observed Mrk 421 in the GeV band from space. Mrk 421 is the brightest extragalactic object in γ -rays in the northern hemisphere (e.g. Gaur et al. 2012a).

Thanks to its proximity, observational studies of Mrk 421 are pervasive throughout the entire EM spectrum. The source has had its radio emission followed over the span of 25 yr at multiple frequencies (Hovatta et al. 2015 and references therein). It has shown rapid and extreme optical variability, including LTV of ~ 4.6 mag (Stein, Odell & Strittmatter 1976), and IDV up to ~ 1.4 mag of brightness change over a very short period (~ 2.5 h) (Guangzhong et al. 1988). Three decades of near infra-red (NIR) data reported by Fan & Lin (1999) provide IDV and STV confirmation of its blazar nature. In 2006, the source was observed with a peak flux ~ 85 mCrab in the 2.0–10.0 keV band, indicating that the first peak of SED occurred at an energy beyond 10 keV (Tramacere et al. 2009; Ushio et al. 2009). There were reports of ‘orphan flares’ (Fraija et al. 2015) in TeV γ -rays (those not having corresponding increased X-ray emission) in Mrk 421 during 2003 and 2004 multiwavelength (MW) campaigns. On 2008 June 10, Super-AGILE detected a hard X-ray flare. MAXI (Monitor of ALL-sky X-ray Image) marked the strongest X-ray flare

in February 2010 ($\sim 164 \pm 17$ mCrab) (Isobe et al. 2015). HESS (High Energy Stereoscopic System) (Aharonian et al. 2005) and MAGIC (Major Atmospheric Gamma Imaging Cherenkov Telescopes) (Albert et al. 2007) observed the time-average high energy spectrum of Mrk 421 during its flaring stages.

The dominant synchrotron self-Compton (SSC) model considers that the same electron population is responsible for the production of soft X-rays and high energy γ -rays. The SSC model agrees with the results of Błażejowski et al. (2005) and Horan et al. (2009), where the fluxes were well correlated with a time lag of less than 1.5 d (MAGIC Collaboration et al. 2016). In 2013 April, Mrk 421 was observed to undergo a major X-ray outburst and was comprehensively investigated by multiple observational facilities, including the *NuSTAR* and *Swift* satellites. Intensive studies of Mrk 421 probing its MW behaviour are numerous (Takahashi et al. 1994; Kerrick et al. 1995; Gupta et al. 2004; Costa et al. 2008; Pittori et al. 2008; Smith et al. 2008; Gaur et al. 2012b; Lico et al. 2012; Blasi et al. 2013; Pian et al. 2014; Paliya et al. 2015; Sinha et al. 2015; Hovatta et al. 2015; Baloković et al. 2016 and references therein). MW campaigns incorporating *Fermi-LAT* gamma-ray detections comprehensively studied Mrk 421 and produced its first ever complete γ -ray continuum during a quiescent state (Abdo et al. 2014). A multidecade optical light curve spanning 1900 to 1991 was extracted by Liu, Liu & Xie (1997) in the *B*-band, suggesting two possible observed time periods of 23.1 ± 1.1 and 15.3 ± 0.7 yr in those flux variations (Sinha et al. 2016). A significant amount of correlation (~ 68 per cent) was found with X-ray data from *RXTE-ASM*, when Tluczykont et al. (2010) studied the long-term very high energy (VHE) light curve of the source. Strong episodes of TeV–X-ray correlation were discussed by Katarzyński et al. (2005). The typical nature of moderate X-ray–GeV flux correlations has been recently examined by Bartoli et al. (2016) through MW observations made from 2008 to 2013.

The least well understood aspect of blazar variability is probably seen on IDV time-scales. To search for and analyse IDV in blazars, we are working on a project in which we study data taken with various ground-based and space-based telescopes (Gupta et al. 2008a,b, 2012, 2016a, 2017; Gaur et al. 2010, 2012a; Gaur et al. 2012b,c, 2015a; Bachev et al. 2012; Agarwal & Gupta 2015; Agarwal et al. 2015, 2016; Kalita et al. 2015; Pandey, Gupta & Wiita 2017). In this paper, we present a study of the IDV of Mrk 421 using the *Chandra* X-ray Observatory (*Chandra*) satellite. We employ all the archival data taken by *Chandra* since its launch, extending from 2000 May 29 to 2015 July 02 (≈ 16 yr) and totalling 72 IDV light curves. This is the most extensive IDV study of Mrk 421 in the X-ray band, covering the longest temporal span. This work provides us with better understanding of the X-ray variability properties of Mrk 421, along with the correlations between hard and soft X-ray bands.

The paper is organized as follows. Section 2 briefly describes the *Chandra* satellite instrumentation along with the methodology for data reduction. Data analysis techniques used to search for flux and spectral variability are discussed in Section 3. Section 4 and Section 5 give our results and a discussion, respectively. Our conclusions are reported in Section 6.

2 CHANDRA X-RAY SATELLITE AND DATA REDUCTION

Launched on 1999 July 23 as a part of the ‘Great Observatories’, this NASA telescope has been a phenomenal tool to study high energy sources such as compact binaries, quasars, and supernovas. *Chandra*’s High Resolution Mirror Assembly typically produces

images with a half-power diameter of the point spread function of <0.5 arcsec. The High Energy Transmission Grating (HETG) and the Low Energy Transmission Grating (LETG) have high resolving powers when compared to their bandwidths and together cover the energy range from ≤ 0.1 to 10 keV. ACIS (Advanced CCD Imaging Spectrometer) and HRC (high resolution camera) are the two in-house focal instruments of the Science Instrument Module (e.g. Weisskopf et al. 2000).

ACIS consists of two CCD arrays: four arrangements of 2×2 arrays, known as ACIS-I (having front-illuminated (FI) CCDs) and six arrangements of 1×6 arrays, ACIS-S (consisting of 4 FI and 2 back-illuminated (BI) CCDs). The time resolution of two ACIS detectors is 3.2 s (e.g. Weisskopf et al. 2000). When observing a wide field ($16' \times 16'$) and/or requiring high energy response, ACIS-I is preferred while imaging observations having a low energy response and a smaller field of view (FoV; $8' \times 8'$) are provided by ACIS-S.

The microchannel plate instrument, HRC, has the fastest time resolution of $16 \mu\text{s}$. It employs two detectors, one of which, HRC-I is calibrated for imaging with a wide FoV of $\sim 30' \times 30'$. The other, HRC-S, is primarily used with the LETG and has a long FoV of $\sim 7' \times 97'$ (e.g. Weisskopf et al. 2000).

2.1 Data Reduction

Mrk 421 was observed by *Chandra* between 2000 May 29 and 2015 July 02, providing a rich set of data for the study of its variable nature in the X-ray energy range of 0.3–10 keV. We downloaded 72 observation IDs from the HEASARC Data Archive.¹ The list of Observation IDs, dates, start times, detectors used, gratings, and exposure times is given in Table 1. The majority of these observations were used for calibration or spectroscopic study of the warm-hot intergalactic medium filaments in the direction of the blazar (e.g. Nicastro et al. 2005; Kaastra et al. 2006; Rasmussen et al. 2007; Yao et al. 2008). Hence, the extensive timing analysis we present here is unique for *Chandra* data.

The *Chandra* Interactive Analysis of Observations (CIAO² version 4.9) package was used in conjunction with CALDB version 4.7.7 to process the data. We first reprocessed the level 2 event file to apply the updated calibration data using the CIAO script *chandra_repro*. We then applied a barycentre correction to the reprocessed level 2 event file using the CIAO tool *axbary*. Out of 72 observations, 48 were done with the ACIS detector and remaining 24 with HRC. Although gratings are used in all these observations, there is a possibility of pile-up in the undispersed (zeroth order) events for a bright source such as Mrk 421 in observations performed with the ACIS detector. The dispersed (first order) events are, however, free from pile-up. So, for the 48 observations taken with ACIS, we determined fluxes from a rectangular region of $800 \text{ arcsec} \times 20 \text{ arcsec}$ that contains only the dispersed source photons. For observations made with HRC, we took a circular region of radius 10 arcsec centred on the source to extract light curves. We have also taken into account the Dead Time Factor (DTF³) while creating the HRC light curves. Finally, the 0.3–10.0 keV light curves were extracted using the CIAO tool *dmextract* with a binning of 500 s. Due to the brightness of Mrk 421, the background contribution is negligible.

¹<https://heasarc.gsfc.nasa.gov/db-perl/W3Browse/w3browse.pl>

²<http://cxc.harvard.edu/ciao/>

³The DTF characterizes the detector's deviation from the standard detection efficiency.

3 ANALYSIS TECHNIQUES

3.1 Excess Variance

Although AGNs in general, and blazars in particular, are generally characterized by rapid X-ray variability, when observed there will be some innate experimental noise. Measurement errors in the light curve (LC) produce finite uncertainties, $\sigma_{\text{err},i}$, for each of the i measurements that contribute additional variance to the observed variance (e.g. Pandey et al. 2017). The quantitative measure of the true variance is known as excess variance and yields the magnitude of variability. Thus, the excess variance is defined for an observed LC having N measured flux values x_i as (Vaughan et al. 2003)

$$\sigma_{XS}^2 = S^2 - \overline{\sigma_{\text{err}}^2}, \quad (1)$$

where S^2 is the total variance of the LC and is given by

$$S^2 = \frac{1}{N-1} \sum_{i=1}^N (x_i - \bar{x})^2 \quad (2)$$

and $\overline{\sigma_{\text{err}}^2}$ is the mean square error and is given by

$$\overline{\sigma_{\text{err}}^2} = \frac{1}{N} \sum_{i=1}^N \sigma_{\text{err},i}^2, \quad (3)$$

where \bar{x} is the arithmetic mean of x_i .

It makes sense to normalize the excess variance

$$\sigma_{NXS}^2 = \sigma_{XS}^2 / \bar{x}^2 \quad (4)$$

and the fractional rms variability amplitude, F_{var} , is defined as

$$F_{\text{var}} = \sqrt{\frac{S^2 - \overline{\sigma_{\text{err}}^2}}{\bar{x}^2}}. \quad (5)$$

It can be shown that the uncertainty in F_{var} is given by (e.g. Vaughan et al. 2003)

$$\text{err}(F_{\text{var}}) = \sqrt{\left(\sqrt{\frac{1}{2N} \frac{\overline{\sigma_{\text{err}}^2}}{\bar{x}^2} F_{\text{var}}}\right)^2 + \left(\sqrt{\frac{\overline{\sigma_{\text{err}}^2}}{N} \frac{1}{\bar{x}}}\right)^2}. \quad (6)$$

3.2 Discrete Correlation Functions

The discrete correlation function (DCF) technique was first introduced to astronomical time series by Edelson & Krolik (1988) and later modified to give better error estimates by Hufnagel & Bregman (1992). The DCF can be used to find possible time lags between bands and so correlate multifrequency AGN LCs data, even when they are distributed irregularly over time, as is typical. Two discrete data trains x and y are taken into account to collect unbinned correlations (unbinned discrete correlation function, UDCF) (e.g. Pandey et al. 2017) via

$$F_{ij} = \frac{(x_i - \bar{x})(y_j - \bar{y})}{\sqrt{(\sigma_x^2)(\sigma_y^2)}}, \quad (7)$$

for the data sets x_i and y_j having \bar{x} and \bar{y} as their mean values, and σ_x and σ_y as their standard deviations, respectively (Gaur et al. 2015b).

In order to obtain a normalized DCF, one must bin the calculated UDCF, but the selected bin size should neither be too large to lose any important data points, nor too small so as to produce spurious correlations. The DCF then can be computed by taking the average

Table 1. Observation log of *Chandra* data for Mrk 421.

Obs ID	Date of observation (dd-mm-yyyy)	Start time (UT) (hh:mm:ss)	Detector	Grating	Exposure time (ks)
1714	29-05-2000	11:39:48	ACIS-S	HETG	19.83
1715	29-05-2000	17:40:11	HRC-S	LETG	19.84
4148	26-10-2002	00:05:02	ACIS-S	LETG	96.84
4149	01-07-2003	14:19:35	HRC-S	LETG	99.98
5318	06-05-2004	14:53:40	ACIS-S	LETG	30.16
5171	13-07-2004	17:19:41	ACIS-S	LETG	67.15
5332	14-07-2004	12:21:48	ACIS-S	LETG	67.06
8378	07-01-2007	23:08:15	ACIS-S	LETG	28.16
6925	08-01-2007	07:12:48	ACIS-S	LETG	27.69
8396	21-01-2007	07:52:59	HRC-S	LETG	29.48
10671	10-10-2009	23:53:51	ACIS-S	LETG	28.96
10664	08-11-2009	05:00:56	ACIS-S	LETG	20.06
11605	16-11-2009	03:43:14	ACIS-S	LETG	5.24
11606	18-11-2009	19:16:47	ACIS-S	LETG	5.24
11607	22-11-2009	09:17:23	ACIS-S	LETG	5.14
11960	02-02-2010	03:31:10	ACIS-I	LETG	20.13
11961	04-02-2010	08:50:00	ACIS-I	LETG	20.17
11962	04-02-2010	14:44:43	ACIS-I	LETG	19.77
11963	06-02-2010	08:54:32	ACIS-I	LETG	20.18
11964	06-02-2010	14:56:02	ACIS-I	LETG	19.77
11967	06-02-2010	20:37:52	ACIS-I	LETG	19.78
10663	13-03-2010	02:11:06	ACIS-S	HETG	15.13
11970	13-03-2010	06:56:51	ACIS-S	LETG	10.07
10665	13-03-2010	10:08:56	HRC-S	LETG	10.15
12121	13-03-2010	13:07:43	ACIS-S	LETG	10.07
10667	13-03-2010	16:14:18	HRC-S	LETG	10.18
10668	13-03-2010	19:13:05	ACIS-S	LETG	10.06
10669	13-03-2010	22:19:39	HRC-S	LETG	10.18
11966	14-03-2010	01:18:27	ACIS-S	LETG	30.06
10670	14-03-2010	10:00:29	ACIS-S	HETG	14.80
12122	10-07-2010	18:37:09	HRC-S	LETG	25.18
13097	16-02-2011	18:33:05	ACIS-S	LETG	30.06
13098	04-07-2011	02:15:37	ACIS-S	HETG	14.80
13099	04-07-2011	06:59:47	ACIS-S	LETG	10.06
13100	04-07-2011	10:12:04	HRC-S	LETG	10.15
13104	04-07-2011	22:07:18	HRC-S	LETG	10.18
13105	05-07-2011	01:06:06	ACIS-S	HETG	15.00
14266	07-04-2012	20:29:18	ACIS-S	LETG	30.05
14320	03-07-2012	11:34:05	ACIS-S	HETG	15.03
14322	03-07-2012	16:07:49	HRC-S	LETG	10.01
14396	03-07-2012	19:09:24	HRC-S	LETG	9.79
14321	03-07-2012	22:06:42	ACIS-S	LETG	10.05
14323	04-07-2012	01:13:05	HRC-S	LETG	10.18
14324	04-07-2012	04:09:45	HRC-S	LETG	9.79
14325	04-07-2012	07:07:03	ACIS-S	LETG	10.05
14326	04-07-2012	10:13:26	HRC-S	LETG	10.19
14397	04-07-2012	13:10:06	HRC-S	LETG	9.79
14327	04-07-2012	16:07:26	ACIS-S	HETG	15.04
15607	07-02-2013	19:15:19	ACIS-S	LETG	30.07
15476	03-04-2013	00:36:24	ACIS-S	LETG	30.05
15477	30-06-2013	16:15:37	ACIS-S	HETG	14.65
15478	30-06-2013	20:46:21	ACIS-S	LETG	10.06
15479	30-06-2013	23:58:37	HRC-S	LETG	10.14
15480	01-07-2013	02:57:24	ACIS-S	LETG	9.76
15481	01-07-2013	05:56:13	HRC-S	LETG	10.19
15482	01-07-2013	08:55:01	ACIS-S	LETG	9.77
15483	01-07-2013	11:53:49	HRC-S	LETG	10.19
15484	01-07-2013	14:52:38	ACIS-S	HETG	14.50
16474	06-03-2014	08:13:12	ACIS-S	LETG	60.07
16424	25-06-2014	13:54:38	ACIS-S	HETG	15.05
16425	25-06-2014	20:44:18	ACIS-S	LETG	10.08
16426	25-06-2014	23:56:09	HRC-S	LETG	10.15
16427	26-06-2014	02:55:01	ACIS-S	LETG	10.08
16428	26-06-2014	06:01:20	HRC-S	LETG	10.18

Table 1 – *continued*

Obs ID	Date of observation (dd-mm-yyyy)	Start time (UT) (hh:mm:ss)	Detector	Grating	Exposure time (ks)
16429	26-06-2014	09:00:09	ACIS-S	LETG	10.08
16430	26-06-2014	12:06:31	HRC-S	LETG	10.17
16431	26-06-2014	15:05:17	ACIS-S	HETG	15.05
17385	01-07-2015	00:42:11	ACIS-S	HETG	15.03
17387	01-07-2015	20:54:30	HRC-S	LETG	10.18
17389	01-07-2015	23:51:09	HRC-S	LETG	10.19
17391	02-07-2015	02:46:19	HRC-S	LETG	10.18
17392	02-07-2015	05:43:39	ACIS-S	HETG	14.06

of a number, M , of UDCF values for each time delay $\Delta t_{ij} = t_j - t_i$ that lie in the range $\tau - \Delta\tau/2 \leq \Delta t_{ij} < \tau + \Delta\tau/2$ as

$$\text{DCF}(\tau) = \frac{1}{M} \sum F_{ij}, \quad (8)$$

with τ being the centre of the time bin $\Delta\tau$. Each bin has a standard error estimate that is given as (Edelson & Krolik 1988)

$$\sigma_{\text{DCF}(\tau)} = \frac{\sqrt{\sum [F_{ij} - \text{DCF}(\tau)]^2}}{M - 1}. \quad (9)$$

The autocorrelation function (ACF) is the special case of the DCF where a data train is correlated with itself ($x = y$), automatically generating a peak at $\tau = 0$. This peak points out the absence of any time lag, and any periodicity in the data would be marked by the presence of other strong peaks (Agarwal & Gupta 2015). Generally, two correlated data signals have a DCF value >0 , while a DCF value <0 indicates that the two data sets are anticorrelated, and a DCF value $= 0$ means that the two data trains have no correlation (Gaur et al. 2014).

3.3 Hardness Ratio

The hardness ratio (HR) is an effective and elementary model-independent method that can simply characterize spectral variations and is defined as

$$\text{HR} = \frac{(H - S)}{(H + S)}, \quad (10)$$

where H is the net count rate in the hard energy band and S is the net count rate in the soft energy band (e.g. Pons et al. 2016). In order to examine spectral variability in our X-ray light curves, we split the LCs into a soft X-ray energy band (0.3–2.0 keV) and a hard X-ray energy band (2.0–10.0 keV) and plotted HR variations with time.

3.4 Duty Cycle

Calculating the duty cycle (DC) gives us a direct estimation of the time fraction for which the object was variable. We determined the DC for Mrk 421 using the definition of Romero, Cellone & Combi (1999), which was thereafter adopted by many authors (e.g. Agarwal et al. 2016). LCs with monitoring sessions of at least 2 h were considered while doing the calculations for

$$\text{DC} = 100 \frac{\sum_{i=1}^n N_i (1/\Delta t_i)}{\sum_{i=1}^n (1/\Delta t_i)} \text{ per cent}, \quad (11)$$

where $\Delta t_i = \Delta t_{i, \text{obs}}(1+z)^{-1}$ is the redshift corrected time duration for which the source was observed having the i^{th} Observation ID. N_i takes the value 1 whenever IDV is detected and is taken to be 0 for no IDV detection. Computation of the DC has been weighted by the actual observing run time Δt_i on the i^{th} night, as the monitoring duration is different for different observations.

4 RESULTS

We have analysed 72 *Chandra* observations of Mrk 421 that provide good data, as tabulated in Table 1. The resulting X-ray LCs are shown in Fig. 1. We have searched for IDV in these LCs and visual inspection of them frequently shows the presence of clear variability (Kalita et al. 2017). We have computed IDV variability parameters in Table 2, which include excess variance, fractional variance (F_{var}), and any time-scales indicated by the ACFs. It is evident that the F_{var} amplitudes of most of the individual observations are considerable, with values exceeding three times the error for the total counts for 65 out of the 72 observations (Paliya et al. 2015; Baloković et al. 2016). Observation ID 11966, taken on 2010 March 14, shows the highest value of variability amplitude (21.31 ± 0.12 per cent) over the entire period and was observed for 30 ks. Whenever possible

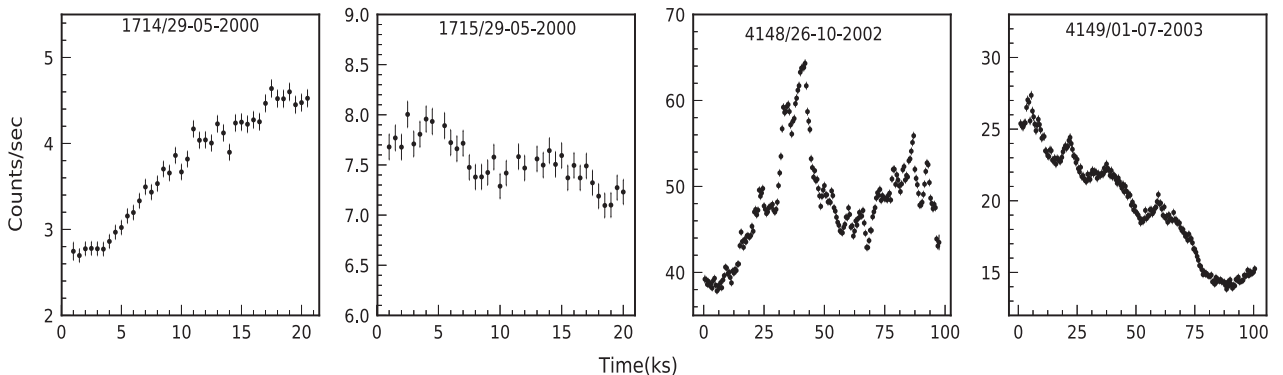


Figure 1. *Chandra* sample light curves of the TeV HBL Mrk 421, labelled with Obs IDs and dates. Full figure appears as supplementary material online only.

Table 2. X-ray variability parameters.

Obs ID	F_{var} (per cent)			ACF (ks)	Bin size (ks)
	Soft (0.3–2keV)	Hard (2–10keV)	Total (0.3–10keV)		
1714	15.24 ± 0.54	18.96 ± 0.54	16.79 ± 0.37	–	1.00
1715 ^a	–	–	2.62 ± 0.30	–	1.00
4148	10.49 ± 0.06	16.27 ± 0.09	12.27 ± 0.05	30.50	3.00
4149 ^a	–	–	18.56 ± 0.07	–	5.00
5318	9.51 ± 0.12	14.62 ± 0.16	11.02 ± 0.09	19.50	1.50
5171	6.02 ± 0.12	9.73 ± 0.19	7.03 ± 0.10	–	5.00
5332	4.35 ± 0.12	8.67 ± 0.21	5.12 ± 0.10	–	3.00
8378	3.77 ± 0.24	4.46 ± 0.49	3.95 ± 0.21	–	2.00
6925	2.15 ± 0.27	4.43 ± 0.49	2.80 ± 0.24	10.07	1.00
8396 ^a	–	–	7.22 ± 0.16	–	2.00
10671	3.94 ± 0.17	5.14 ± 0.26	4.32 ± 0.14	14.98	1.00
10664	2.54 ± 0.18	2.39 ± 0.31	2.21 ± 0.16	–	1.00
11605	1.67 ± 0.35	1.66 ± 0.56	2.07 ± 0.32	–	0.60
11606	1.11 ± 0.40	0.23 ± 2.66	0.86 ± 0.47	–	0.60
11607	1.04 ± 0.45	3.14 ± 0.62	1.41 ± 0.33	–	0.70
11960	7.27 ± 0.36	10.56 ± 0.53	8.21 ± 0.29	–	2.00
11961	7.45 ± 0.26	10.55 ± 0.31	8.26 ± 0.19	–	2.00
11962	4.16 ± 0.28	5.77 ± 0.39	4.66 ± 0.22	10.07	1.00
11963	4.08 ± 0.24	4.03 ± 0.30	3.65 ± 0.20	–	2.00
11964	1.32 ± 0.37	3.97 ± 0.34	3.13 ± 0.22	–	2.00
11967	5.80 ± 0.38	8.11 ± 0.52	8.55 ± 0.30	–	2.00
10663	2.33 ± 0.36	4.36 ± 0.30	3.60 ± 0.23	–	0.60
11970	2.11 ± 0.28	4.52 ± 0.43	2.48 ± 0.20	–	1.00
10665 ^a	–	–	0.59 ± 0.40	–	0.60
12121	7.13 ± 0.23	13.42 ± 0.37	8.43 ± 0.21	–	1.00
10667 ^a	–	–	5.71 ± 0.22	–	1.00
10668	7.84 ± 0.20	10.72 ± 0.29	8.45 ± 0.17	–	1.00
10669 ^a	–	–	2.59 ± 0.25	–	1.00
11966	18.70 ± 0.15	27.95 ± 0.22	21.31 ± 0.12	–	3.00
10670	2.52 ± 0.55	4.37 ± 0.50	3.66 ± 0.35	–	1.00
12122 ^a	–	–	2.54 ± 0.54	–	2.00
13097	6.42 ± 1.09	7.93 ± 2.47	6.28 ± 0.95	–	2.00
13098	5.13 ± 0.75	4.14 ± 0.81	4.78 ± 0.56	–	1.00
13099	2.48 ± 0.51	2.72 ± 1.00	1.65 ± 0.45	–	1.00
13100 ^a	–	–	2.07 ± 0.49	–	1.00
13104 ^a	–	–	1.69 ± 0.48	–	1.00
13105	4.21 ± 0.68	6.21 ± 0.65	4.56 ± 0.46	–	2.00
14266	3.28 ± 0.41	4.93 ± 0.73	3.33 ± 0.35	5.51	1.00
14320	3.57 ± 0.95	6.11 ± 0.99	4.33 ± 0.66	–	1.00
14322 ^a	–	–	2.68 ± 0.43	–	1.00
14396 ^a	–	–	0.86 ± 0.64	–	1.00
14321	1.45 ± 0.59	2.33 ± 1.25	1.06 ± 0.62	–	1.00
14323 ^a	–	–	2.52 ± 0.42	–	1.00
14324 ^a	–	–	2.53 ± 0.40	–	1.00
14325	1.21 ± 0.62	1.04 ± 2.11	0.84 ± 0.69	–	1.00
14326 ^a	–	–	8.98 ± 0.34	–	1.00
14397 ^a	–	–	1.19 ± 0.44	–	1.00
14327	5.11 ± 0.60	7.86 ± 0.62	6.16 ± 0.44	–	1.00
15607	6.87 ± 0.19	10.98 ± 0.31	7.65 ± 0.15	9.51	1.00
15476	10.05 ± 0.16	16.73 ± 0.23	12.03 ± 0.13	–	1.00
15477	5.44 ± 0.42	8.60 ± 0.40	7.09 ± 0.28	–	1.00
15478	7.63 ± 0.30	10.60 ± 0.49	8.45 ± 0.22	–	1.00
15479 ^a	–	–	4.52 ± 0.26	–	1.00
15480	1.87 ± 0.33	2.86 ± 0.61	2.00 ± 0.29	–	1.00
15481 ^a	–	–	2.52 ± 0.29	–	1.00
15482	0.51 ± 0.61	1.40 ± 0.79	0.74 ± 0.43	–	1.00
15483 ^a	–	–	5.07 ± 0.28	–	1.00
15484	3.41 ± 0.49	5.44 ± 0.46	4.58 ± 0.31	–	1.00
16474	9.59 ± 0.09	12.12 ± 0.13	10.38 ± 0.07	–	5.00
16424	7.77 ± 0.70	12.88 ± 0.69	10.67 ± 0.48	–	1.00
16425	3.29 ± 0.50	3.70 ± 0.91	3.10 ± 0.41	–	1.00
16426 ^a	–	–	3.82 ± 0.40	–	1.00
16427	2.09 ± 0.47	1.19 ± 1.30	2.00 ± 0.43	–	1.00
16428 ^a	–	–	3.39 ± 0.41	–	1.00

Table 2 – *continued*

Obs ID	F_{var} (per cent)		ACF (ks)	Bin size (ks)
	Soft (0.3–2keV)	Hard (2–10keV)		
16429	6.65 ± 0.44	9.31 ± 0.74	–	1.00
16430 ^a	–	–	–	1.00
16431	1.59 ± 1.11	1.67 ± 1.06	–	1.00
17385	7.03 ± 0.75	7.25 ± 0.73	–	1.00
17387 ^a	–	–	–	1.00
17389 ^a	–	–	–	1.00
17391 ^a	–	–	–	1.00
17392	4.78 ± 0.55	7.57 ± 0.52	–	1.00

^aObservation done with HRC detector in which the light curve cannot be split into different energy bands; hence, the values of F_{var} are not quoted for soft and hard energy bands.

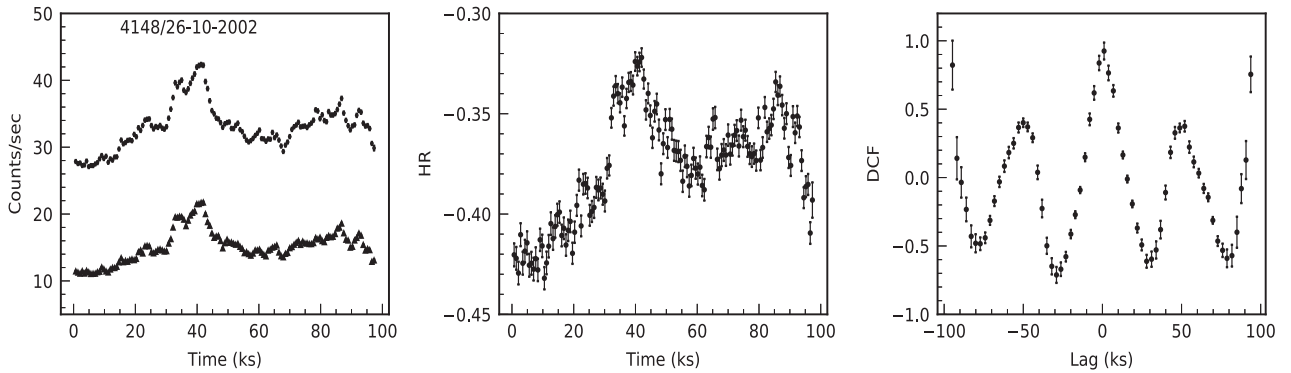


Figure 2. Soft (0.3–2 keV, denoted by filled circles) and hard (2–10keV, denoted by filled triangles) LCs are in the left-hand panel, HR is in the middle panel, and the DCF between soft and hard LCs comprises the right-hand panel. Corresponding observation ID of Mrk 421 and the date are marked in the left-hand panel. The observations are restricted to ACIS detectors as the HRC detector does not have an energy column and thus cannot be separated into soft and hard energy bands. Full figure appears as supplementary material online only.

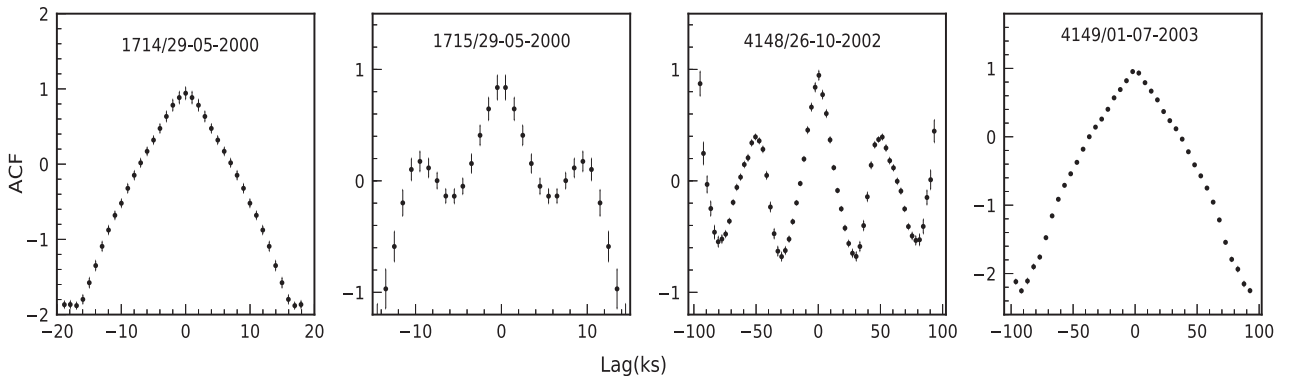


Figure 3. ACF plots for sample LCs of the blazar Mrk 421. Full figure appears as supplementary material online only.

(for ACIS data only), we split the X-ray light curves into two energy bands: the soft X-ray energy band spans 0.3–2.0 keV, while the hard band is taken as 2.0–10.0 keV. The fractional variances separately calculated for hard and soft bands are also given in Table 2; this data provides evidence for the hard band being more variable than the soft band (for 41 out of 48 observations). Statistically valid variations from Mrk 421 are clearly indicated by F_{var} computations. These allowed us to compute the DC of our source to be ~ 84 per cent, showing a strong presence of X-ray IDV.

Fig. 2 displays the LCs of the soft and hard energy bands, both of which are shown in the left-hand panels, with HR plots in the middle panels and DCF results between the hard and soft LCs displayed in the right-hand panels. The HRs plotted against time show

clear indications of spectral variations. The DCF plots quantify the strong positive correlation between the hard and soft bands, at least whenever considerable variability is present. We fitted each DCF plot with a Gaussian function ($y = A \exp(-(x - x_0)^2/w)$), with amplitude A , central value x_0 , and width, w to estimate any possible time lag, and found a time lag almost equal to zero in each case. These results suggest that both soft and hard bands are emitted from the same region at the same time (e.g. Pandey et al. 2017).

The ACF plots are displayed in Fig. 3, and they provide strong evidence of variability time-scales for seven observation IDs. The time-scales are taken from the locations of significant non-zero peaks in the ACF. For seven plots, such time-scales range from 5.5 to 30.5 ks and are presented in Table 2. The remaining ACF plots

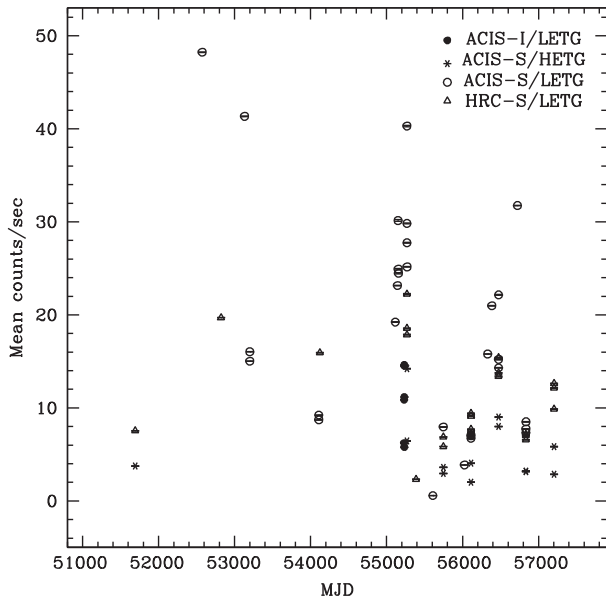


Figure 4. Long-term X-ray variability in Mrk 421.

either exhibit such a high noise level that any variability time-scales cannot be ascertained or simply do not indicate the presence of any variability (Gupta et al. 2016b).

The course of this entire set of *Chandra* observations of Mrk 421 spans over 16 yr. The LTV LC of the mean of the total X-ray fluxes is shown in Fig. 4. Very substantial variations, ranging up to 21.31 ± 0.12 percent, are seen in the individual observational count rates. The LTV count rates vary from 0.396 ± 0.004 to 48.226 ± 0.023 , clearly emphasizing how variable this blazar is. No clear patterns can be discerned from a visual inspection of these LTV data.

In Fig. 5, we show plots of the HR against flux. This spectral index–flux representation was studied to uncover patterns in the HR as a function of 0.3–10.0 keV count rates for different time intervals. Spectral evolution of Mrk 421 during this ≈ 16 yr of observation is clearly marked by changing relative strength of particle acceleration and synchrotron cooling processes in X-ray emitting regions (Kalita et al. 2015). The presence of clockwise or anticlockwise loops in this spectral hardness–flux plot reveals information about the leading emission mechanism during that particular period. For these HR against count rate plots, we considered the entire set of 48 observations made with ACIS for which the HR can be measured and if we detected any loop in the plot, we considered that segment as one epoch and started a search for subsequent loops. This way, we found eight distinct epochs having either clockwise or anticlockwise loops that include a substantial majority of the observations (31 of 48). X-ray emissions can be understood as arising from high energy relativistic particles that are accelerated as a result of shocks propagating in the relativistic jets. When these accelerated particles come in contact with the inhomogeneous magnetic fields, significant synchrotron emission extends into the X-ray band, which will dominate the cooling process. Fig. 5 contains an anticlockwise loop for Epoch 1, which can be understood as a hard lag (Zhang et al. 2002). This leads us to conclude that particles were being accelerated to very high speeds during that time span (Kalita et al. 2015). Dominance of particle acceleration mechanisms was again indicated in Epoch 3. Epochs 4 and 7 also have anticlockwise loops, providing evidence for particles being accelerated in the internal

shocks as they outflow along the jets. Clockwise loops, or soft lags, were displayed by Epochs 2 and 5 and then again by Epochs 6 and 8. This implies that the synchrotron cooling mechanism dominated the X-ray emission in those particular periods.

5 DISCUSSION

An important route to understanding the emission mechanisms in blazars and other AGN involves careful measurement of strong flux variations on diverse time-scales. Studies of rapid variability of blazars have also helped us to determine the key properties of the emitting region such as its size, location, and structure (e.g. Stein et al. 1976; Ciprini et al. 2003; Gupta et al. 2016b). Whenever extreme variability is combined with relatively weak spectral features, as in BL Lac objects, it has long been accepted that a relativistic jet close to the LOS is emitting the continuum; this results in the dramatic increase in the brightness of the observed radiation and a reduction of the observed variability time-scales due to Doppler boosting (Blandford & Rees 1980; Ulrich et al. 1997). The high X-ray variations displayed by many blazars could arise either directly from the synchrotron emission or through Compton scattering of the lower energy synchrotron photon (SSC) process, again supporting the idea of relativistic bulk motion in blazars (Hoyle & Burbidge 1966; Bassani & Dean 1983). In general, intrinsic AGN emission and variability can occur through two fundamental theoretical branches, either the purely relativistic-jet-based models (Marscher & Gear 1985; Gopal-Krishna & Wiita 1992; Marscher 2014; Calafut & Wiita 2015) or the accretion-disc-based models (Chakrabarti & Wiita 1993; Mangalam & Wiita 1993). IDV and STV in radio-quiet quasars, and perhaps in certain blazars, if they are in very low states, can possibly be explained through instabilities present in accretion discs (Mangalam & Wiita 1993). Yet any such accretion-disc-based model does not provide a satisfactory explanation for the very strong and rapid variability on most time-scales that can be much more easily provided by the Doppler-boosted radiations from relativistic jets (Chakrabarti & Wiita 1993).

An adiabatic shock-in-jet model can nicely explain blazar variability on LTV time-scales (Marscher & Gear 1985; Wagner & Witzel 1995). The model describes relativistic shocks as arising from disturbances created in the inner portion of the jet that can quickly steepen into shocks. As they propagate through the jet, these shocks create major flux. Additional fluctuations are observed when these shocks interact with helical jet structures, by changing the effective viewing angle and hence Doppler factor (Camenzind & Krockenberger 1992; Gopal-Krishna & Wiita 1992; Pandey et al. 2017). Relativistic jets also suffer some turbulence behind some of the shock regions, which can be held responsible for smaller STV and IDV (Marscher 2014; Calafut & Wiita 2015; Pollack, Pauls & Wiita 2016).

Some blazars, such as Mrk 421, exhibit flaring TeV emissions on the time-scales of a few minutes, which can be short when compared to the light crossing time of the SMBH of those blazars. Also, for TeV seed photons to escape from their source region, which is quite compact, it appears that the Lorentz factor of the emitting region needs to be $\gtrsim 50$. This is required in order to avoid absorption via pair production through interaction with soft radiation fields, but such extreme Lorentz factors are hard to achieve with a jet with a uniform bulk flow. The flaring states of Mrk 421 might be more naturally explained via a ‘jets-in-a-jet’ model proposed by Gianios, Uzdensky & Begelman (2009). This ‘jets-in-a-jet’ model can explain the origin of TeV emission along with fast X-ray variability

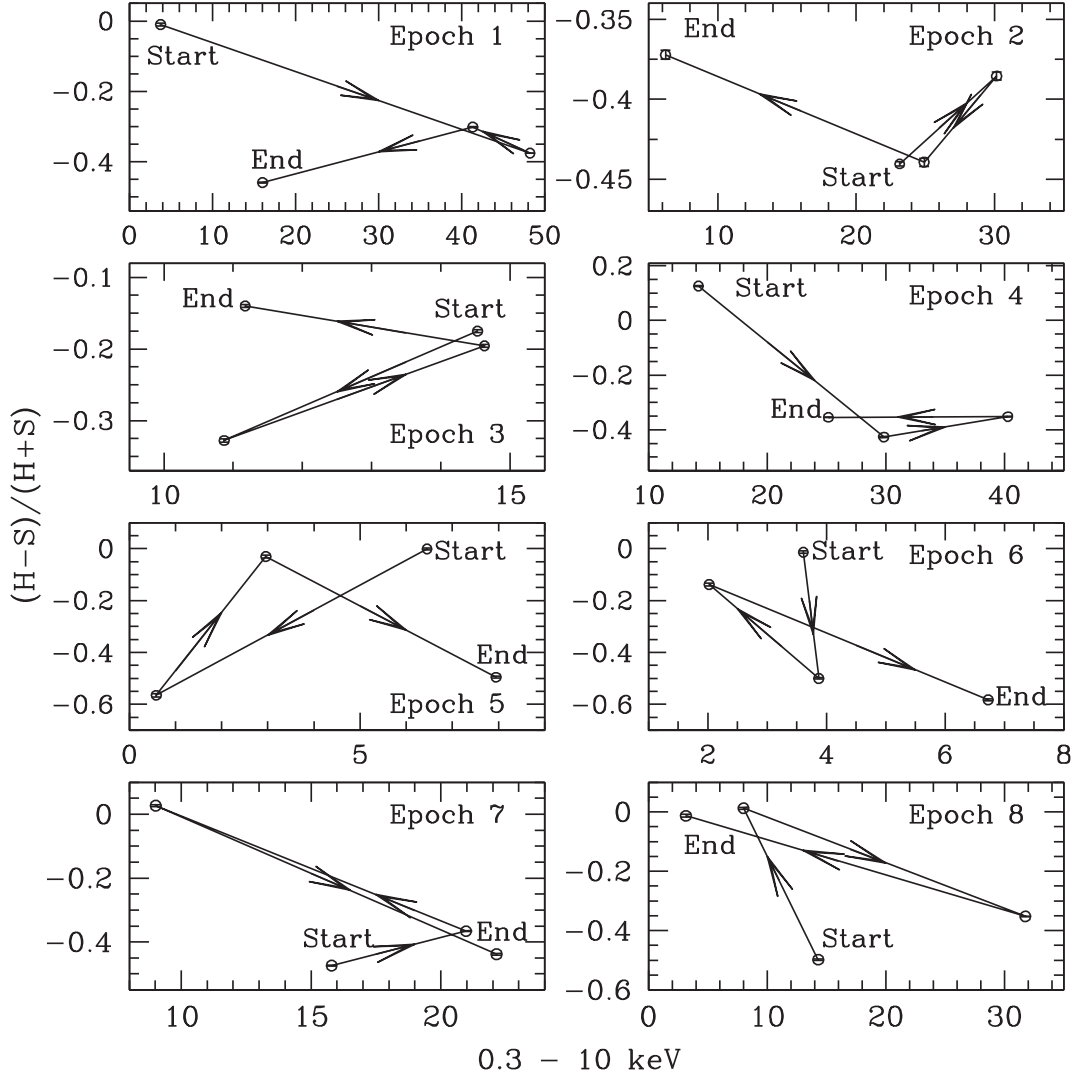


Figure 5. Spectral variations of Mrk 421 in various epochs with start and end points marking the loop directions. Each epoch corresponds to the time interval during which the data were acquired for each loop, considered from Epoch 1 to Epoch 8: Epoch 1: 29-05-2000 to 13-07-2004; Epoch 2: 08-11-2009 to 02-02-2010; Epoch 3: 04-02-2010 to 06-02-2010; Epoch 4: 13-03-2010 to 14-03-2010; Epoch 5: 14-03-2010 to 04-07-2011; Epoch 6: 05-07-2011 to 03-07-2012; Epoch 7: 07-02-2013 to 30-06-2013; and Epoch 8: 01-07-2013 to 25-06-2014.

though production of rapid flares arising from the ultrarelativistic outflow of material from magnetic reconnection sites. The presence of multiple reconnection regions and the phenomena related to the rupturing of a large reconnection site make this model more flexible so that the production of more slowly varying flares is also possible. Electrons accelerated within the jets would be responsible for rapid hard X-ray variability and the successive flares detected in Mrk 421. This phenomena can also yield the observed spectral hardening at high energies.

Certain parameters can be estimated, rather independently of model details, by assuming that synchrotron emission is responsible for the X-ray emission from HBLs, such as Mrk 421. In the observer's frame, the acceleration time-scale of the diffuse shock acceleration mechanism (Blandford & Eichler 1987), assumed to be the way in which electrons are accelerated, is given as (Zhang et al. 2002)

$$t_{\text{acc}}(\gamma) \simeq 3.79 \times 10^{-7} \frac{(1+z)}{\delta} \xi B^{-1} \gamma_s, \quad (12)$$

where ξ is defined as the acceleration parameter, B is the magnetic field, and γ is the Lorentz factor of the electrons. Synchrotron emission is also believed to be the origin of the X-ray emission, when TeV blazars are considered. An individual electron with energy $E = \gamma m_e c^2$ has a synchrotron cooling time-scale of

$$t_{\text{cool}}(\gamma) \simeq 7.74 \times 10^8 \frac{(1+z)}{\delta} B^{-2} \gamma^{-1} \text{s}. \quad (13)$$

For the *Chandra* energy range, the critical synchrotron emission frequency $\nu \simeq 4.2 \times 10^6 \frac{\delta}{1+z} B \gamma^2 = 10^{18} \nu_{18} \text{ Hz}$.

Although the minimum variability time-scale found in this work is 5.5 ks, the variability associated with that observation is only ~ 3 per cent, so we took 9.51 ks as the shortest clear variability time-scale, as F_{var} exceeds 7 per cent for it. The cooling time-scale should be greater than or equal to the minimum variability time-scale or ~ 9.51 ks for Mrk 421 in this work. This implies

$$B \geq 0.30(1+z)^{1/3} \delta^{-1/3} \nu_{18}^{-1/3} \text{G}. \quad (14)$$

Although a range of values for δ for Mrk 421 between 20 and 50 (e.g. Tavecchio, Maraschi & Ghisellini 1998; Abdo et al. 2011; Zhu et al. 2016, and references therein) appear in the literature, we choose $\delta = 25$ (e.g. Baloković et al. 2016) and get

$$B \geq 0.10 v_{18}^{-1/3} \text{G}. \quad (15)$$

Combining these values of B and δ , we estimate the electron Lorentz factor as

$$\gamma \geq 3.06 \times 10^5 v_{18}^{2/3}. \quad (16)$$

The characteristic radius of emitting region can also be evaluated using the bound

$$R \leq \frac{ct_{\text{var}}\delta}{1+z} \leq 6.92 \times 10^{15} \text{cm}. \quad (17)$$

Relativistic electrons directly responsible for hard, variable X-ray emission, as are investigated by *Chandra*, must be repeatedly accelerated because of the short cooling time-scales of these very high-energy electrons (Pandey et al. 2017). These electrons must be injected via one or more of the various possible acceleration mechanisms mentioned above. We note that diffusive-shock acceleration could be responsible both for variations in the flux and spectral hardening at high energies.

For this HBL, we probed the X-ray spectral variability by analysing the HR, as it serves as an easy and efficient way to understand changes in the spectra; however, the physical parameters that are responsible for spectral variability are not directly evaluated by this method. We observed that for Mrk 421, the HR increases as the flux (count rate) increases, or, as the flux is increasing, the spectrum tends to get flatter. Thus, it seems that this source is following the general trend of ‘hardens-when-brighter’ of the HBL type blazar as discussed previously (Pian et al. 1998; Zhang et al. 2002; Brinkmann et al. 2003; Ravasio et al. 2004; Pandey et al. 2017). The spectral hardness–flux analysis we conducted provides a model-independent approach to understanding the spectral variations of the source. The presence of anticlockwise loops in the plots indicates that the soft band leads the hard band (or there is a hard lag between the two emissions), i.e. with the increase in the total flux of the source, the hard flux usually increases more than the soft flux. This indicates that the particle acceleration mechanism is predominantly responsible for the observed X-ray emission during that particular period of time (Bhagwan et al. 2016). When any clockwise loop (or soft lag) occurs in the HR against flux plot, the soft flux increases more than the hard flux with increasing total flux. In these epochs, the hard band leads the soft band, as is the case when the synchrotron emission mechanism temporarily dominates the acceleration mechanism.

6 CONCLUSIONS

We studied 72 *Chandra* light curves of the TeV blazar Mrk 421 and searched for variability time-scales of IDV. The rapid X-ray variability studied here most likely originates within compact regions of the relativistic jet. Our conclusions are summarized as follows:

(i) The fractional variability amplitude provides a clear indication of variability on many occasions, with highest variability amplitude being over 21 per cent. The variability in hard energy X-ray bands presumably originates from a compact region within a relativistic jet.

(ii) The DC for these variations is at least ≈ 84 per cent, which indicates that the source was exceptionally variable in the observed 16-yr span.

(iii) We found evidence for time-scales ranging from 5.5 to 30.5 ks in 7 LCs of Mrk 421 using the ACF technique. Other observations have noisier ACF plots in which variability time-scales are not clearly present. Using the shortest strong variability time-scale of 9.51 ks, we can estimate key parameters in a fashion that is essentially independent of the theoretical model. We find a magnetic field $B > 0.10 v_{18}^{-1/3}$ G, electron Lorentz factor $\gamma \geq 3.06 \times 10^5 v_{18}^{2/3}$, and radius of the emitting region $R \leq 6.92 \times 10^{15}$ cm.

(iv) The DCF technique was applied to the hard (2–10 keV) and soft (0.3–2 keV) X-ray bands and displayed positive correlations with no time lag. This implies that the emission in both nearby bands arose from the same production region at the same time; i.e. there is no evidence that the softer X-rays arise from synchrotron emission while the harder come from SSC.

(v) An HR analysis was also employed to study spectral variations. HRs showed flatter spectra at high fluxes (Fig. 2). This indicated that the HR normally increased with increasing flux and got ‘harder-when-brighter’. Fig. 5 displays more information about the spectral evolution of the source. During these extended observations, a few epochs had hard lags, pointing to the particle acceleration mechanism being responsible for the X-ray emissions, whereas a few epochs had soft lags, indicating that X-rays are predominantly emitted by the synchrotron cooling mechanism during those periods.

ACKNOWLEDGEMENTS

We thank the referee for constructive comments and suggestions. This research has made use of data obtained from the *Chandra* Data Archive and the *Chandra* Source Catalog, and software provided by the *Chandra* X-ray Center (CXC) in the application packages CIAO, CHIPS, and SHERPA.

The work of VA, ACG, and KKY is supported by BRNS-DAE (Board of Research in Nuclear Sciences – Department of Atomic Energy), Government of India funded project No. 37(3)/14/17/2014-BRNS. ZZ is thankful for support from the Chinese Academy of Sciences Hundred-Talented program (Y787081009). PJW is grateful for hospitality at the Kavli Institute for Particle Astrophysics and Cosmology, Stanford University, and Shanghai Astronomical Observatory during a sabbatical.

REFERENCES

- Abdo A. A. et al., 2011, *ApJ*, 736, 131
 Abdo A. A. et al., 2014, *ApJ*, 782, 110
 Abeysekara A. U. et al., 2017, *ApJ*, 841, 100
 Agarwal A., Gupta A. C., 2015, *MNRAS*, 450, 541
 Agarwal A. et al., 2015, *MNRAS*, 451, 3882
 Agarwal A. et al., 2016, *MNRAS*, 455, 680
 Aharonian F. et al., 2005, *A&A*, 430, 865
 Albert J. et al., 2007, *ApJ*, 669, 862
 Bachev R., Semkov E., Strigachev A., Gupta A. C., Gaur H., Mihov B., Boeva S., Slavcheva-Mihova L., 2012, *MNRAS*, 424, 2625
 Baloković M. et al., 2016, *ApJ*, 819, 156
 Bartoli B. et al., 2016, *ApJS*, 222, 6
 Bassani L., Dean A. J., 1983, *Space Sci. Rev.*, 35, 367
 Bhagwan J., Gupta A. C., Papadakis I. E., Wiita P. J., 2016, *New Astron.*, 44, 21
 Blandford R., Eichler D., 1987, *Phys. Rep.*, 154, 1
 Blandford R. D., Rees M. J., 1980, *Phys. Scr.*, 17, 265
 Blasi M. G. et al., 2013, *A&A*, 559, A75
 Błażejowski M. et al., 2005, *ApJ*, 630, 130
 Brinkmann W., Papadakis I. E., den Herder J. W. A., Haberl F., 2003, *A&A*, 402, 929
 Calafut V., Wiita P. J., 2015, *J. Astrophys. Astron.*, 36, 255

- Camenzind M., Krockenberger M., 1992, *A&A*, 255, 59
- Chakrabarti S. K., Wiita P. J., 1993, *ApJ*, 411, 602
- Ciprini S., Tosti G., Raiteri C. M., Villata M., Ibrahimov M. A., Nucciarelli G., Lanteri L., 2003, *A&A*, 400, 487
- Costa E. et al., 2008, *Astron. Telegram*, 1574
- Edelson R. A., Krolik J. H., 1988, *ApJ*, 333, 646
- Fan J. H., Lin R. G., 1999, *ApJS*, 121, 131
- Finke J. D., Becker P. A., 2014, *ApJ*, 791, 21
- Fraija N., Cabrera J. I., Benítez E., Hiriart D., 2015, preprint ([arXiv:1508.01438](https://arxiv.org/abs/1508.01438))
- Gaur H., Gupta A. C., Lachowicz P., Wiita P. J., 2010, *ApJ*, 718, 279
- Gaur H., Gupta A. C., Wiita P. J., 2012a, *AJ*, 143, 23
- Gaur H. et al., 2012b, *MNRAS*, 420, 3147
- Gaur H. et al., 2012c, *MNRAS*, 425, 3002
- Gaur H., Gupta A. C., Wiita P. J., Uemura M., Itoh R., Sasada M., 2014, *ApJ*, 781, L4
- Gaur H. et al., 2015a, *MNRAS*, 452, 4263
- Gaur H. et al., 2015b, *A&A*, 582, A103
- Giannios D., Uzdensky D. A., Begelman M. C., 2009, *MNRAS*, 395, L29
- Gopal-Krishna Sagar R., Wiita P. J., 1993, *MNRAS*, 262, 963
- Gopal-Krishna Wiita P. J., 1992, *A&A*, 259, 109
- Guangzhong X., Ruwei L., Yuan Z., Pengjin H., Yun Z., Xiaoyu L., Xinde L., Jianxin W., 1988, *A&AS*, 72, 163
- Gupta A. C., Banerjee D. P. K., Ashok N. M., Joshi U. C., 2004, *A&A*, 422, 505
- Gupta A. C., Fan J. H., Bai J. M., Wagner S. J., 2008a, *AJ*, 135, 1384
- Gupta A. C. et al., 2008b, *AJ*, 136, 2359
- Gupta A. C. et al., 2012, *MNRAS*, 425, 1357
- Gupta A. C. et al., 2016a, *MNRAS*, 458, 1127
- Gupta A. C., Kalita N., Gaur H., Duorah K., 2016b, *MNRAS*, 462, 1508
- Gupta A. C. et al., 2017, *MNRAS*, 465, 4423
- Horan D. et al., 2009, *ApJ*, 695, 596
- Hovatta T. et al., 2015, *MNRAS*, 448, 3121
- Hoyle F., Burbidge G. R., 1966, *ApJ*, 144, 534
- Hufnagel B. R., Bregman J. N., 1992, *ApJ*, 386, 473
- Isobe N. et al., 2015, *ApJ*, 798, 27
- Kaastra J. S., Werner N., Herder J. W. A. d., Paerels F. B. S., de Plaa J., Rasmussen A. P., de Vries C. P., 2006, *ApJ*, 652, 189
- Kalita N., Gupta A. C., Wiita P. J., Bhagwan J., Duorah K., 2015, *MNRAS*, 451, 1356
- Kalita N., Gupta A. C., Wiita P. J., Dewangan G. C., Duorah K., 2017, *MNRAS*, 469, 3824
- Katarzyński K., Ghisellini G., Tavecchio F., Maraschi L., Fossati G., Maticchiadis A., 2005, *A&A*, 433, 479
- Kerrick A. D. et al., 1995, *ApJ*, 438, L59
- Lico R. et al., 2012, *A&A*, 545, A117
- Liu F. K., Liu B. F., Xie G. Z., 1997, *A&AS*, 123, 569
- MAGIC Collaboration et al., 2016, *A&A*, 593, A91
- Mangalam A. V., Wiita P. J., 1993, *ApJ*, 406, 420
- Marcha M. J. M., Browne I. W. A., Impey C. D., Smith P. S., 1996, *MNRAS*, 281, 425
- Marscher A. P., 2014, *ApJ*, 780, 87
- Marscher A. P., Gear W. K., 1985, *ApJ*, 298, 114
- Miller H. R., Carini M. T., Goodrich B. D., 1989, *Nature*, 337, 627
- Nicastro F. et al., 2005, *ApJ*, 629, 700
- Paliya V. S., Böttcher M., Diltz C., Stalin C. S., Sahayanathan S., Ravikumara C. D., 2015, *ApJ*, 811, 143
- Pandey A., Gupta A. C., Wiita P. J., 2017, *ApJ*, 841, 123
- Pian E. et al., 1998, *ApJ*, 492, L17
- Pian E. et al., 2014, *A&A*, 570, A77
- Pittori C. et al., 2008, *Astron. Telegram*, 1583
- Pollack M., Pauls D., Wiita P. J., 2016, *ApJ*, 820, 12
- Pons E., Elvis M., Civano F., Watson M. G., 2016, *ApJ*, 824, 51
- Punch M. et al., 1992, *Nature*, 358, 477
- Rasmussen A. P., Kahn S. M., Paerels F., Herder J. W. d., Kaastra J., de Vries C., 2007, *ApJ*, 656, 129
- Ravasio M., Tagliaferri G., Ghisellini G., Tavecchio F., 2004, *A&A*, 424, 841
- Rees M. J., 1984, *ARA&A*, 22, 471
- Romero G. E., Cellone S. A., Combi J. A., 1999, *A&AS*, 135, 477
- Schubnell M. et al., 1993, in Leahy D. A., Hicks R. B., Venkatesan D., eds, 23rd International Cosmic Ray Conference Vol. 1. World Scientific, Singapore, p. 409
- Sinha A., Shukla A., Misra R., Chitnis V. R., Rao A. R., Acharya B. S., 2015, *A&A*, 580, A100
- Sinha A. et al., 2016, *A&A*, 591, A83
- Smith A. J. et al., 2008, in Caballero R., D’Olivo J. C., Medina-Tanco G., Nellen L., Sanchez F.A., Valdes-Galicia J. F., eds, 30th International Cosmic Ray Conference Vol. 3. Universidad Nacional Autónoma de México, Mexico City, Mexico, p. 973
- Stein W. A., Odell S. L., Strittmatter P. A., 1976, *ARA&A*, 14, 173
- Stoeckle J. T., Morris S. L., Gioia I. M., Maccacaro T., Schild R., Wolter A., Fleming T. A., Henry J. P., 1991, *ApJS*, 76, 813
- Takahashi T. et al., 1994, *IAU Circ.*, 5993
- Tavecchio F., Maraschi L., Ghisellini G., 1998, *ApJ*, 509, 608
- Ulaczyk M., H.E.S.S. Collaboration, 2010, in Rieger F. M., van Eldik C., Hofmann W., eds, 25th Texas Symposium on Relativistic Astrophysics. p. 197
- Tramacere A., Giommi P., Perri M., Verrecchia F., Tosti G., 2009, *A&A*, 501, 879
- Ulrich M. H., Maraschi L., Urry C. M., 1997, *Annu. Rev. Astron. Astrophys.*, 35, 445
- Urry C. M., Padovani P., 1995, *PASP*, 107, 803
- Ushio M. et al., 2009, *ApJ*, 699, 1964
- Vaughan S., Edelson R., Warwick R. S., Uttley P., 2003, *MNRAS*, 345, 1271
- Wagner R., 2008, in Aharonian F. A., Hofmann W., Rieger F., eds, AIP Conf. Ser. Vol. 1085, High Energy Gamma-ray Astronomy. Am. Inst. Phys., New York. p. 399
- Wagner S. J., Witzel A., 1995, *ARA&A*, 33, 163
- Weisskopf M. C., Tananbaum H. D., Van Speybroeck L. P., O’Dell S. L., 2000, in Truemper J. E., Aschenbach B., eds, Proc. SPIE Vol. 4012, X-Ray Optics, Instruments, and Missions III. SPIE, Bellingham, p. 2
- Yao Y., Nowak M. A., Wang Q. D., Schulz N. S., Canizares C. R., 2008, *ApJ*, 672, L21
- Zhang Y. H. et al., 2002, *ApJ*, 572, 762
- Zhu Q., Yan D., Zhang P., Yin Q.-Q., Zhang L., Zhang S.-N., 2016, *MNRAS*, 463, 4481

SUPPORTING INFORMATION

Supplementary data are available at [MNRAS](https://www.mnras.org) online.

Figure 1. *Chandra* sample light curves of the TeV HBL Mrk 421, labelled with Obs IDs and dates.

Figure 2. Soft (0.3–2 keV, denoted by filled circles) and hard (2–10 keV, denoted by filled triangles) LCs are in the left-hand panel, hardness ratio is in the middle panel, and the DCF between soft and hard LCs comprises the right-hand panel. Corresponding observation ID of Mrk 421 and the date are marked in the left-hand panel. The observations are restricted to ACIS detectors as the HRC detector does not have an energy column and thus cannot be separated into soft and hard energy bands.

Figure 3. Autocorrelation function (ACF) plots for sample LCs of the blazar Mrk 421.

Please note: Oxford University Press is not responsible for the content or functionality of any supporting materials supplied by the authors. Any queries (other than missing material) should be directed to the corresponding author for the article.

This paper has been typeset from a \LaTeX file prepared by the author.